

# Linear-Response and Real-Time Time-Dependent Density Functional Theory Studies of Core-Level Near-Edge X-Ray Absorption

K. Lopata,<sup>\*,†</sup> B. E. Van Kuiken,<sup>‡</sup> M. Khalil,<sup>‡</sup> and N. Govind<sup>\*,†</sup>

<sup>†</sup>William R. Wiley Environmental Molecular Sciences Laboratory, Pacific Northwest National Laboratory, Richland, Washington 99352, United States

<sup>‡</sup>Department of Chemistry, University of Washington, Seattle, Washington 98195, United States

**ABSTRACT:** We discuss our implementation and application of time-dependent density functional theory (TDDFT) to core-level near-edge absorption spectroscopy, using both linear-response (LR) and real-time (RT) approaches. We briefly describe our restricted excitation window TDDFT (REW-TDDFT) approach for core excitations, which has also been reported by other groups. This is followed by a detailed discussion of real-time TDDFT techniques tailored to core excitations, including obtaining spectral information through delta-function excitation, postprocessing time-dependent signals, and resonant excitation through quasi-monochromatic excitation. We present results for the oxygen K-edge of water and carbon monoxide; the carbon K-edge of carbon monoxide; the ruthenium L<sub>3</sub>-edge for the hexaammineruthenium(III) ion, including scalar relativistic corrections via the zeroth order regular approximation (ZORA); and the carbon and fluorine K-edges for a series of fluorobenzenes. In all cases, the calculated spectra are found to be in reasonable agreement with experimental results, requiring only a uniform shift ranging from −4 eV to +19 eV, i.e., on the order of a few percent of the excitation energy. Real-time TDDFT visualization of excited state charge densities is used to visually examine the nature of each excitation, which gives insight into the effects of atoms bound to the absorbing center.

## 1. INTRODUCTION

Core-level X-ray absorption spectroscopy (XAS) is a powerful and versatile class of techniques for probing the electronic and geometric structure of matter at the atomic level. In XAS, electrons are excited from a core state of an atom to bound valence or continuum states in energetically distinct absorption edges. It is convention to label these edges according to the origin core state (K-edge for 1s, L<sub>1</sub>-edge for 2s, L<sub>2</sub>-edge for 2p<sub>1/2</sub>, L<sub>3</sub>-edge for 2p<sub>3/2</sub>, etc). The spectroscopy of absorptions near the rising edge, typically referred to as XANES, involves excitations from the core state to increasingly high energy virtual states, which gives insight into the chemical state of the atom (e.g., oxidation state, coordination, bonding, etc). Absorption at energies sufficient to cause ejection of a photoelectron, with subsequent scattering off nearby atoms, is termed EXAFS and gives structural information about neighboring atoms (e.g., identity, distances, coordination/solvent shells, etc).<sup>1,2</sup>

From a theoretical standpoint, XANES and EXAFS are usually treated distinctly. In EXAFS, where the spectral “ripples” arise from modulation of X-ray absorption due to backscattering from nearby atoms, the essential physical quantities are the scattering amplitude and phase shifts, from which the spectrum is typically computed using a damped spherical photoelectron wave function approximation. These quantities, which were once only obtainable from experiments on well-characterized crystals, are now routinely computed using Green’s function formalisms with localized (“muffin tin”) potentials and have been very successful in modeling EXAFS spectra. For discussion of theoretical approaches to XAS, see refs 1–4. From a first principles modeling standpoint, these

techniques are especially powerful when used in conjunction with ab initio molecular dynamics simulations.<sup>5,6</sup>

XANES, on the other hand, involves subionization threshold excitations and thus requires a full treatment of the electronic structure of the absorbing center and neighbors. Here, an ab initio approach is especially promising as it naturally captures all transitions within the absorbing atom, as well as interactions with the chemical environment, on equal footing. Core holes, which are highly localized on a single atom, are often well described with single determinant theories.<sup>1,2</sup> Here, one popular approach is the static exchange approximation (STEX), which is akin to configuration interaction singles (CIS) using relaxed final core-hole orbitals.<sup>7,8</sup> There has also been much recent progress in applying various density functional theory (DFT)-based techniques, which can be broadly categorized into time-dependent and static (time-independent) methods. Static methods incorporate the relaxation of the core-hole and valence orbitals through indirect means such as manual preparation of a partially occupied core-hole state (typically a half-occupied core) and/or use of modified core potentials that mimic the relaxation.<sup>9–12</sup> The absorption spectra are then computed via the transition dipole elements between initial and final states of interest. These approaches are advantageous in that they capture the electronic relaxation of the core-hole and valence states, provided that the initial states and/or potentials are properly chosen. Time-dependent DFT methods, on the other hand, are extensions of TDDFT to core level excitations<sup>13–16</sup> and require no special preparation of core holes or potentials. One drawback of

Received: July 3, 2012

Published: August 17, 2012

TDDFT-based methods, however, is that although they excel at predicting relative excitation energies, e.g., peak separations in a given spectrum or trends within a series of molecules, the absolute energies and the quality of the spectra are often highly dependent on the exchange-correlation functional, and thus spectra typically must be shifted by a constant to match experimental results.

From a practical standpoint, TDDFT must be tailored somewhat, as naive application of linear response TDDFT (LR-TDDFT) requires computing a large number of irrelevant roots (i.e., valence excitations) before obtaining core excitations. One very effective LR-TDDFT technique is a windowed solver,<sup>13–16</sup> which computes only excitations within a narrow energy range. Another approach is to use real-time TDDFT (RT-TDDFT), which has the distinct advantage that a system's full absorption spectrum can be computed in just one simulation (three in the absence of symmetry), including all excitations from core to valence. In this paper, we outline the working principles of LR-TDDFT and RT-TDDFT as applied to core states (section 2) and present X-ray absorption spectra calculations on a selection of small molecules, a ruthenium complex treated with scalar relativity, and a series of fluorobenzenes (section 3). Core excitations via RT-TDDFT have been studied before,<sup>17</sup> but to our knowledge this is the first completely general implementation of RT-TDDFT for core states. Finally, we summarize our results in section 4.

## 2. COMPUTATIONAL APPROACH

**2.1. Linear-Response TDDFT for Core-Level Excitations.** Over the past decade, LR-TDDFT, in conjunction with suitable exchange-correlation functionals, has become a computationally attractive approach for studying excited-state spectra in a wide range of molecular and materials systems. Since there are several comprehensive reviews of TDDFT and the relevant working equations,<sup>18–24</sup> we only give a brief description here. In short, the excitation energies within LR-TDDFT are obtained as solutions to the non-Hermitian eigenvalue equation:

$$\begin{pmatrix} \mathbf{A} & \mathbf{B} \\ \mathbf{B}^* & \mathbf{A}^* \end{pmatrix} \begin{pmatrix} \mathbf{X} \\ \mathbf{Y} \end{pmatrix} = \omega \begin{pmatrix} \mathbf{1} & \mathbf{0} \\ \mathbf{0} & -\mathbf{1} \end{pmatrix} \begin{pmatrix} \mathbf{X} \\ \mathbf{Y} \end{pmatrix} \quad (1)$$

where the matrices  $\mathbf{A}$  and  $\mathbf{B}$  are given by

$$A_{a\sigma, b\tau} = \delta_{ij} \delta_{ab} \delta_{\sigma\tau} (\epsilon_{a\sigma} - \epsilon_{i\tau}) + \Lambda_{a\sigma, b\tau} \quad (2)$$

$$B_{a\sigma, j\tau} = \Lambda_{a\sigma, j\tau} \quad (3)$$

In the above equations  $i, j, \dots$  represent occupied orbitals;  $a, b, \dots$  represent virtuals;  $\sigma$  and  $\tau$  represent the spin indices; and  $\epsilon$  represents the eigenvalues.  $\Lambda$  is the interaction kernel given by

$$\Lambda_{a\sigma, j\tau} = (a_{\sigma} i_{\sigma} | j_{\tau} b_{\tau}) + (a_{\sigma} i_{\sigma} | w_{\sigma\tau} | j_{\tau} b_{\tau}) \quad (4)$$

where

$$w_{\sigma\tau} \equiv \frac{\delta^2 E_{xc}}{\delta \rho_{\sigma}(\mathbf{r}) \delta \rho_{\tau}(\mathbf{r}')}$$

is the second derivative response from the exchange-correlation functional. Within the Tamm-Dancoff approximation (TDA),<sup>20</sup> the above eigenvalue equation reduces to the Hermitian equation  $\mathbf{A}\mathbf{X} = \omega\mathbf{X}$ , which is formally similar to CIS with redefined Coulomb and exchange integrals. Our implementation in NWChem<sup>19,20,25,26</sup> is based on the iterative subspace

Davidson algorithm,<sup>19–23</sup> which is an efficient approach for valence excitations. Core excitations, on the other hand, are computationally expensive because the full excitation matrices have to be constructed and subsequently diagonalized, or in other words, one has to calculate a large number of roots. Formally, the numerical cost of diagonalizing the full TDDFT equations scales as  $O(N^6)$ , because of the tetradic nature of the RPA matrix.<sup>27</sup> To overcome this issue, we have implemented a restricted excitation window approach (REW-TDDFT) where calculations are performed within a smaller subspace of single excitations involving excitations from the relevant core orbitals. This simple solution is valid because the core excitations are well-separated from the valence-to-valence transitions. Similar implementations have also been reported and validated by other groups.<sup>13–16</sup> To account for relativistic effects in the core excitation energies, we have used scaled ZORA eigenvalues.<sup>28–30</sup>

**2.2. Real-Time TDDFT for Core-Level Excitations.** In real-time TDDFT, rather than solving for discrete roots, the electronic wave function or density matrix is explicitly propagated in time under the influence of the time-dependent Fock matrix.<sup>17,31–42</sup> In a Gaussian atom-centered basis set, it is more convenient to work with density matrices, where the analog of the time-dependent Schrödinger equation is the von Neumann equation

$$i \frac{\partial \mathbf{P}(t)}{\partial t} = [\mathbf{F}(t), \mathbf{P}(t)] \quad (5)$$

where  $\mathbf{P}(t)$  is the density matrix,  $\mathbf{F}(t)$  is the Fock matrix, and the prime denotes matrices in the molecular orbital (MO) basis. In the most general case of hybrid DFT, the Fock matrix is given by

$$\begin{aligned} \mathbf{F}[\mathbf{P}(t)] = & \mathbf{H}^{\text{core}} + \mathbf{G}^J[\mathbf{P}(t)] + \alpha \mathbf{G}^K[\mathbf{P}(t)] \\ & + \beta \mathbf{G}^{\text{X-DFT}}[\rho(\mathbf{r}, t)] + \gamma \mathbf{G}^{\text{C-DFT}}[\rho(\mathbf{r}, t)] \\ & - \mathbf{D} \cdot \mathbf{E}(t) \end{aligned} \quad (6)$$

where  $\rho(\mathbf{r}, t)$  is the time-dependent electron density; the  $\alpha$ ,  $\beta$ , and  $\gamma$  coefficients quantify the admixture of DFT and Hartree–Fock (HF) exact exchange;  $\mathbf{D}$  is the dipole matrix; and  $\mathbf{E}(t)$  includes all applied electric fields. Note, this assumes dipolar coupling with the external field, with an implicit assumption that the wavelength of the photon is much larger than the system size. This approximation, however, can break down for very high energy core states, e.g., K-edge of transition metals, where the X-ray wavelengths are on the order of Ångströms. Going beyond requires higher order coupling, e.g., quadrupoles.<sup>43,44</sup> For all results presented here, eq 5 is integrated using a second order Magnus propagator

$$\mathbf{P}'(t + \Delta t) = e^{-i\mathbf{F}'(t+\Delta t/2)\Delta t} \mathbf{P}'(t) e^{i\mathbf{F}'(t+\Delta t/2)\Delta t} \quad (7)$$

where  $\Delta t$  is the time step, and the Fock matrix at the future time is guessed via linear extrapolation followed by self-consistent iterative interpolation. For more details about Magnus propagators, see refs 41, 42, and 45. When capturing core excitations, which typically have oscillation periods on the order of a few attoseconds, very small time steps must be taken to ensure accuracy, usually a few tenths of an attosecond or less.

Since  $\mathbf{P}(t)$  yields complete dynamical information about the system under arbitrary external electric fields, core spectra are naturally captured using a spectroscopic real-time approach. A useful technique for obtaining spectra is to excite the system

## Real-time TDDFT analysis of carbon monoxide core excitations

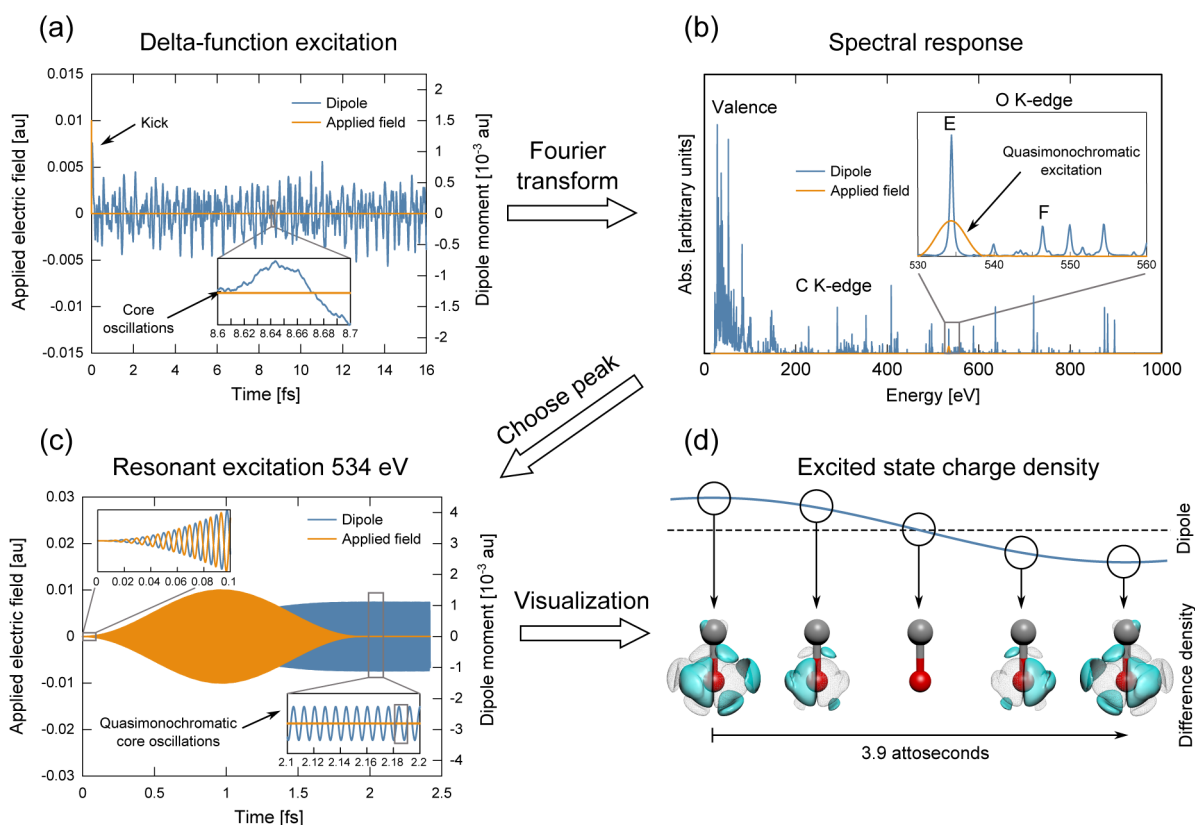


**Figure 1.** Real-time TDDFT analysis of carbon monoxide core excitations, focused on a particular  $x$ -polarized (transverse) oxygen K-edge absorption. (a) Time-dependent dipole moment after an  $x$ -polarized delta-function excitation. (b) The resulting absorption spectrum after Fourier transform and spectral range of a quasi-monochromatic  $x$ -polarized excitation tuned to the peak of interest in the K-edge (labeled peak E). (c) Time-dependent applied field and dipole moment for the quasi-monochromatic resonant excitation. (d) Charge density difference snapshots (blue positive, wireframe negative) at an oscillation maximum of the electronic wavepacket after resonant excitation.

with a nonphysical delta-function electric field perturbation which simultaneously excites all electronic modes from valence to core:

$$\mathbf{E}_\delta(t) = \kappa \delta(t) \hat{\mathbf{d}} \quad (8)$$

where  $\kappa$  is the kick strength and  $d = x, y, z$  is the kick polarization. See Figure 1a for an example of the time-dependent dipole moment  $\mu(t)$  in carbon monoxide after an  $x$ -polarized delta-function excitation (discussed in detail in section 3.1). Note that, overall, the dipole signals from such excitations are typically dominated by the valence response, and the core oscillations are of relatively small amplitude and extremely short period. The complex-valued molecular polarizability is obtained from the Fourier transform of the resulting  $\mu(t)$

$$\alpha_{d,j}(\omega) = \frac{1}{\kappa} \tilde{\mu}_{d,j}(\omega) \quad (9)$$

where  $j = x, y, z$  is the “measurement” polarization. In the absence of magnetic fields, the off-diagonals of the  $3 \times 3$  tensor  $\alpha(\omega)$  can be neglected, and thus, assuming no molecular symmetry, three simulations are required to compute the polarizability. Finally, the absorption spectrum (dipole strength function) is

$$S(\omega) = \frac{4\pi\omega}{3c} \text{Tr}[\text{Im}[\alpha(\omega)]] \quad (10)$$

as shown in Figure 1b. In the limit of small  $\kappa$ , the resulting spectrum is identical to that obtained using linear-response TDDFT. Although a delta function has a theoretically infinite bandwidth, due to sampling, the spectrum is only valid for frequencies less than  $\pi/\Delta t$ . Since core excitations involve much higher frequencies than valence excitations, extra care must be taken to choose a sufficiently small  $\Delta t$  to avoid sampling errors. Finally, since core excitations are often tiny, rapid oscillations buried in the full dipole time signal, in order to ensure a clean spectrum, it is often important to postprocess the time-dependent dipole moment,  $\mu(t)$ , by multiplying by a function  $w(t)$  before taking the Fourier transform, which accelerates convergence of the transform, i.e., reduces required simulation time  $t_{\text{max}}$ . The simplest is exponential damping of the form:

$$w_D(t) = e^{-t/\tau} \quad (11)$$

where  $\tau$  is the exponential damping time constant. In the infinite time signal limit, this results in uniformly Lorentzian broadened peaks with half-width at half-maximum (HWHM) of  $(1/\tau)^{1/2}$ . For especially “busy” signals run for short times, e.g., Figure 1a, a windowing function is useful for extracting the spectrum. Though selection of an optimal window function is an art in itself, for our purposes we found that a Hann window offers good performance in the core region for resolving peaks with similar frequencies and heights

$$w_H(t) = \sin^2(\pi/\sigma[t - t_0]) \quad (12)$$



For preprocessing purposes, typically one picks  $t_0 = t_{\max}/2$  and  $\sigma = t_{\max}$ .

As a final point about spectral calculations, often relativistic effects are important for core excitations, in which case all electron methods like the zeroth order regular approximation (ZORA) are useful. In the context of RT-TDDFT, incorporating ZORA involves adding a time-independent contribution to the one-electron part of the Fock matrix (eq 6). One subtle point is that in ground state calculations, scaled ZORA eigenvalues are used to match four-component calculations.<sup>28,30</sup> For consistency, in RT-TDDFT one could either scale the time-dependent density matrix before computing the time-dependent dipole moment, or more simply, adjust the computed absorption spectrum. In practice, the correction to the ZORA eigenvalues is effectively constant over the eigenvalues in the narrow core region of interest, and thus a RT-TDDFT spectrum can simply be shifted by this frequency-independent constant as a postprocessing step.

A complementary RT-TDDFT technique is resonant excitation, where the molecule is subject to a monochromatic laser pulse tuned to a particular resonance. Visualization of the resulting excited state electron density gives insight into the nature of the excitation. Since this visualization includes the density matrix phase information, it gives a truer representation of the excited state than either static orbital pictures or transition difference densities. Put another way, transition difference densities are frequency-dependent quantities which effectively illustrate the time-averaged charge dynamics for a particular excitation, whereas real-time snapshots show the nature of the charge dynamics (i.e., charge oscillations) during the course of an excitation. Moreover, as it captures the full electronic response, RT-TDDFT resonant excitation can model excited states in the nonlinear (beyond perturbation) regime. Because infinite time (continuous wave) simulations are impractical, these excitations are typically taken to be a finite enveloped pulse. These types of excitations, however, are only quasi-monochromatic, and the spectral width, i.e., the range of frequencies excited, is inversely proportional to the width in time. Thus, exciting a spectrally isolated peak requires only a short pulse with potentially only a few oscillations, while selectively exciting a peak buried in a “busy” spectrum requires a long pulse. In the context of core excitations, the excitation energies are typically on the order of hundreds or thousands of electronvolts, yet spaced by only a few electronvolts, thus requiring a long envelope with many oscillations in order to have an excitation with adequately narrow spectral width. Although a Gaussian window is a natural choice, we have found that for core resonant excitations, a Hann envelope is more a efficient choice since it starts and decays smoothly from exactly zero, unlike a Gaussian which formally has infinite extent and thus introduces significant spectral artifacts due to truncation effects, i.e., the finite propagation time. In practice, a Hann excitation window offers a good compromise between low side-lobe intensities at the cost of slightly increased spectral width. This envelope takes the form:

$$\mathbf{E}_R(t) = \kappa w_H(t) \sin(\omega_0 t) \hat{\mathbf{d}} \quad (13)$$

where  $w_H(t)$  is defined in eq 12. As an example, Figure 1b shows the spectral range of a quasi-monochromatic Hann pulse exciting field overlaid on the absorption spectrum, with the corresponding time-dependent applied field and dipole in Figure 1c. After excitation, the system is in a coherent superposition between the ground and target excited state,

i.e., an electronic wavepacket consisting of these two states, as shown by the monochromatic oscillations. Snapshots of the difference density  $\rho(\mathbf{r},t) - \rho_0(\mathbf{r})$  are shown in Figure 1d, where blue represents charge buildup relative to the ground state, and wireframe represents charge depletion. For clearer visualization, often  $\rho_0$  is taken to be the middle of the oscillation rather than the  $t = 0$  value.

One potential alternative to the resonant excitation method is to prepare the density matrix such that the system is placed directly into the excited state of interest. If done improperly, however, this can introduce an undefined quantity of energy to the system and result in nonphysical relaxation dynamics from this step-like perturbation from the ground state.

### 3. RESULTS

In this section, we present (LR/RT)-TDDFT core spectra for water, carbon monoxide, a simple prototypical ruthenium complex, and a range of fluorobenzenes and compare with experimental spectra. All TDDFT calculations were performed using a development version of NWChem.<sup>25,26</sup> The experimental spectrum for water was digitized from ref 46. The data for carbon monoxide were digitized from ref 47, and the fluorobenzene data digitized from ref 48. The  $[\text{Ru}(\text{NH}_3)_6]^{3+}$  complex experimental data were digitized from ref 49.

In general and as expected, we found that the absolute positions of the TDDFT spectra were highly dependent on the choice of exchange-correlation functional, with increasing Hartree–Fock (HF) admixture giving rise to increasingly blue-shifted spectra. In some cases (e.g., water), hybrid functionals with stronger HF content like Becke Half-and-Half<sup>50</sup> (50% HF) gave the best absolute agreement with experimental results, while in other cases (e.g., the ruthenium complex) B3LYP<sup>51</sup> was best. In the context of core excitations, unlike with valence excitations,<sup>52</sup> range-separated functionals (e.g., CAM-B3LYP<sup>53</sup>) offer little improvement as the excitations are highly local. The absolute spectral positions, however, are far less important than the relative heights and spacings of the spectral features, and in this regard we found that B3LYP gave the best overall agreement with experimental results. In this light, and for the sake of comparison, all calculations presented below exclusively use the B3LYP functional. We used the Sapporo basis sets,<sup>54,55</sup> where higher polarization functions were required to capture higher energy postedge excitation, which involve higher energy virtual states. As with the exchange-correlation, there was also a shift in the spectra due to basis choice. As such, the TDDFT spectra were shifted to match experimental results to compensate for the combined XC and basis shifts. Moreover, there is increasing deviation from experimental results for the higher lying excitations, which results from basis set effects and inadequacies of the functional to reproduce Rydberg or continuum states. An alternate approach is to use a plane-wave basis set, which overcomes the limitations of atom-centered basis sets for describing continuum states.<sup>56</sup>

Before moving on to the results, peak broadening deserves a brief discussion. As formulated, TDDFT does not include damping and thus cannot compute peak linewidths or lineshapes without phenomenological inputs. As such, in this paper most linear-response results are presented as unbroadened stick spectra whose heights are the oscillator strengths in atomic units. The real-time results, on the other hand, are intrinsically broadened by virtue of the finite simulation time and further broadened by the windowing. It is important to

note, however, that since no damping is included in the propagation, these widths are completely artificial, and in the limit of infinite time propagation without windowing postprocessing, the spectra are expected to become stick spectra with peak magnitudes identical to the linear-response data. To verify this (results not shown), for a few cases we explicitly checked that for long-time propagation followed by exponential damping in time domain (i.e., convolution with a Lorentzian in frequency domain) before the Fourier transform, the real-time spectra agreed perfectly with the corresponding linear-response spectrum Lorentzian broadened by the same time constant. For a better qualitative agreement with experimental results, especially for excitations to higher lying virtual orbitals, energy-dependent broadening is often applied to theoretical spectra, but for clarity we present only uniformly broadened spectra, which offers a more honest representation of the quality of the calculations.

**3.1. K-Edge Calculations on Water and Carbon Monoxide.** First, we present K-edge (excitation from 1s orbital) core absorption calculations on water and carbon monoxide and compare the results with gas phase experiments. In this section, all geometries were optimized in the gas phase using the aug-cc-pVTZ basis and the B3LYP exchange correlation functional, and all excited state calculations used the Sapporo-QVP<sup>54,55</sup> basis with added diffuse functions and B3LYP.

Figure 2 shows computed and experimental<sup>46</sup> oxygen K-edge absorption spectra for gas-phase water. The linear-response

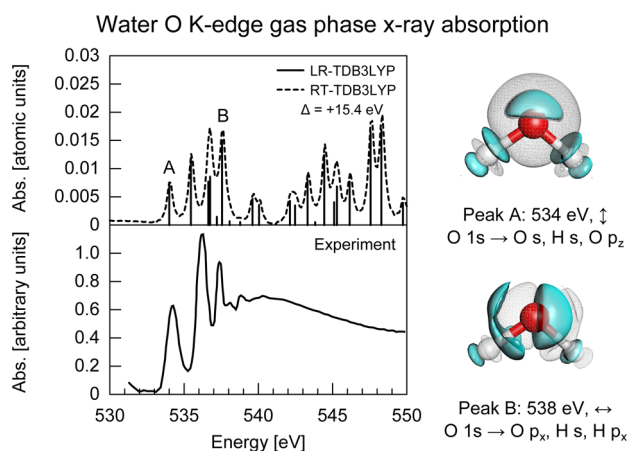


**Figure 2.** Left: (LR/RT)-TDB3LYP calculated oxygen K-edge absorption spectra, along with gas-phase experimental results. Right: Charge density difference snapshots (blue positive, wireframe negative) at an oscillation maximum for two electronic wavepackets after resonant excitation (isovalue  $9 \times 10^{-7}$  au). z-polarized peak A and x-polarized peak B are both dominated largely by oscillations around the oxygen atom, with little influence from the hydrogen atoms. Experimental data were digitized from ref 46.

TDDFT roots (solid) with oscillator strengths are shown in atomic units along with the equivalent real-time TDDFT absorption spectrum (dashed). Each RT-TDDFT delta function (eq 8) simulation had a kick strength of  $\kappa = 0.01$  au, a time step of  $\Delta t = 0.02$  au =  $4.8 \times 10^{-4}$  fs, and simulation time of  $t_{\text{max}} = 500$  au = 12 fs. The time signal was exponentially damped (eq 11) with  $\tau = 120$  fs = 2.9 fs before the Fourier transform, and the magnitude scaled for comparison with the LR values. Both LR and RT spectra were shifted by  $\Delta = +15.4$  eV to match the experimental spectrum (bottom) at the lowest

energy excitation (peak A). Since the RT simulation is in the weak-perturbation limit, the RT and LR spectra match perfectly. Overall, there is reasonable agreement between theory and experiment, and (REW-LR/RT)-TDDFT both capture the near-edge features well. Although water is a simple molecule with largely atom-like core excitations, it is nevertheless illustrative to examine a few of the excitations in detail. The two figures on the right of Figure 2 show snapshots of the excited state difference density  $\rho(\mathbf{r},t) - \rho_0(\mathbf{r})$  at an oscillation maximum after resonant excitation. Positive deviation is shown in blue, while negative deviation is shown in wireframe. Peak A, which was excited with a z-polarized (up–down on figure) Hann pulse (eq 13) with  $\omega_0 = 534$  eV, maximum  $\kappa = 0.01$  au, center  $t_0 = 50$  au = 1.2 fs, and width of  $\sigma = 2t_0$ , shows clear z oscillations around the oxygen atom, accumulation of charge in the O  $p_z$ , and very little contribution from the hydrogen atoms. Peak B, with  $\omega_0 = 538$  eV and x polarization (same Hann parameters as peak A), likewise shows x oscillations, buildup in virtual O  $p_x$  (note radial node), and minimal influence of the hydrogen atoms.

Figure 3 shows the carbon K-edge data for carbon monoxide, derived from the procedure outlined in Figure 1. Since CO has

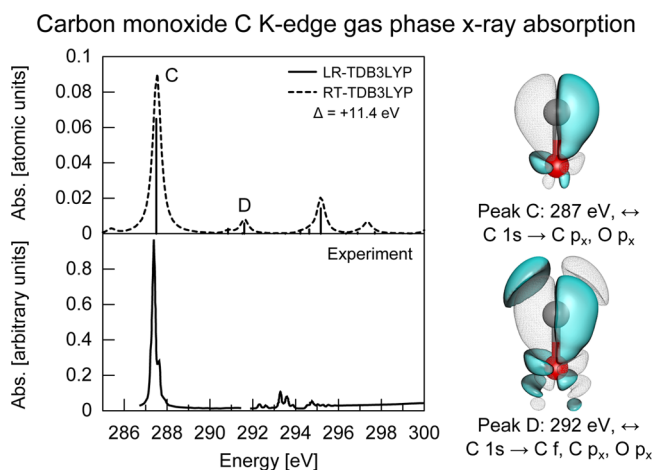


**Figure 3.** Left: (LR/RT)-TDB3LYP calculated carbon K-edge absorption spectra for carbon monoxide, along with experimental gas-phase spectrum. Right: Charge density difference snapshots (blue positive, wireframe negative) at an oscillation maximum for two electronic wavepackets after resonant excitation. Peak C (snapshot isovalue  $3 \times 10^{-5}$  au) shows clear C  $p_x$  character, with contributions from the oxygen atom. Peak D (snapshot isovalue  $2 \times 10^{-6}$  au) is similar, only to a higher virtual orbital and has C f contributions. Experimental data were digitized from ref 47.

symmetry, only two polarizations of  $\delta$ -function simulation were needed. Here, the LR and RT spectra were both shifted by  $\Delta = +11.4$  eV to match with experimental results.<sup>47</sup> The relatively simple spectrum is dominated by the absorption at  $\sim 287.4$  eV (peak C), which corresponds to a C  $1s \rightarrow \pi^*$  (C  $p_x$ , O  $p_x$ ) x-polarized transition. The influence of the oxygen atom is clearly visible in the excited state charge density after resonant excitation (Hann pulse,  $\kappa = 0.01$  au,  $t_0 = 80$  au = 1.9 fs,  $\sigma = 2t_0$ ,  $\omega_0 = 287$  eV). Here, there is out-of-phase charge density above and below the bond axis, which is indicative of excitation to a  $\pi^*$  state. Peak D, which is higher in the C K-edge at  $\sim 291.6$  eV, is qualitatively similar to peak C but only corresponds to an excitation to a higher virtual orbital. There are clear C f contributions visible as out-of-phase lobes, and also increased

contribution from the oxygen atom. The oxygen K-edge absorption for CO (shifted by  $\Delta = +14.6$  eV) is shown in Figure 4. The spectrum is likewise quite simple and dominated

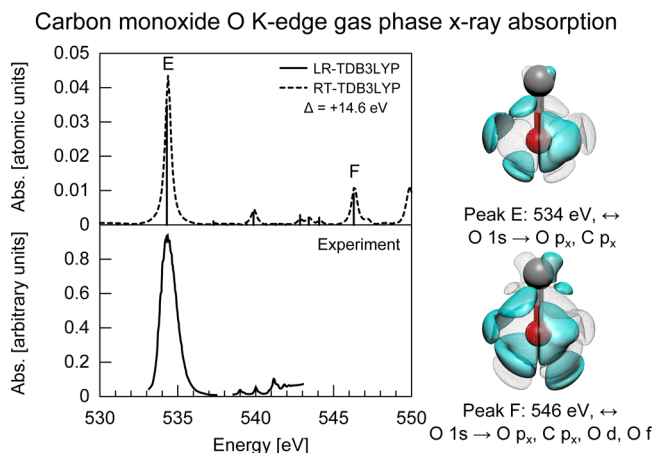


**Figure 4.** Left: (LR/RT)-TDB3LYP spectra along with experimental data for the oxygen K-edge absorption of carbon monoxide. Right: Charge density difference snapshots (blue positive, wireframe negative) for two electronic wavepackets after resonant excitation. Peak E (isovalue  $3 \times 10^{-6}$  au) shows a localized excitation around the oxygen atom, and similarly for peak F (isovalue  $6 \times 10^{-7}$  au), which is an analogous excitation, only to a higher virtual orbital. Experimental data were digitized from ref 47.

by the  $\sim 534.4$  eV strong  $\pi$ -polarized O  $1s \rightarrow \pi^*$  transition. Here, unlike the C K-edge case, the excited state density for peak E (Hann pulse,  $\kappa = 0.01$  au,  $t_0 = 40$  au = 0.97 fs,  $\sigma = 2t_0$ ,  $\omega_0 = 534$  eV) shows that the carbon atom has only a small influence on this excitation, which is largely confined to the space around the oxygen atom. Excitation to a higher virtual (peak F) shows that it is still largely oxygen-like, with a nodal structure as well as some increase in carbon content.

**3.2. Ruthenium  $L_3$ -Edge in  $[\text{Ru}(\text{NH}_3)_6]^{3+}$ .** Next, we consider the  $L_3$ -edge absorption spectra for  $[\text{Ru}(\text{NH}_3)_6]^{3+}$ , a prototypical Ru(III) complex which has been extensively studied.<sup>2,57,58</sup> Relativistic effects are significant in Ru, and experimentally spin-orbit splitting gives rise to a higher energy  $L_2$ -edge ( $2p_{1/2}$ ) and a lower energy  $L_3$ -edge ( $2p_{3/2}$ ). In this study, we neglect spin-orbit splitting but do account for scalar relativistic effects using the zeroth order regular approximation (ZORA). The selection rules for the  $L_3$ -edge are very similar to excitation from 2p orbitals treated in a scalar relativistic fashion, and we thus compare our calculations directly to the experimental  $L_3$ -edge data. In essence, in the atomic  $J$ - $J$  coupling picture, transitions obey a  $\Delta J = 0, \pm 1$  dipole selection rule. This means that transitions at the  $L_3$ -edge are allowed to all d orbitals, both those of  $d_{3/2}$  and  $d_{5/2}$  character. In a spin-free picture, all p  $\rightarrow$  d transitions are dipole allowed, yielding the same selection rule. Moreover, ligand field multiplet calculations have shown that spin-orbit coupling does not strongly influence  $L_3$ -edges,<sup>58</sup> and there have been several examples where spin-free DFT has successfully reproduced Ru  $L_3$ -edges.<sup>59,60</sup>

The geometry was optimized using the ORCA code<sup>61</sup> in an implicit COSMO water solvent at 20 °C ( $\epsilon = 80.4$ ), with B3LYP and the def2-SVP basis with the associated ECP (WMB28). All (LR/RT)-TDDFT calculations were performed using NWChem using B3LYP, the 6-31G\* basis for the ligands,

and the Sapporo-DK3-TVP basis for Ru with G-functions removed. The RT delta-function kick simulation used  $\kappa = 0.1$  au,  $\Delta t = 0.006$  au =  $1.5 \times 10^{-4}$  fs, and  $t_{\text{max}} = 200$  au = 4.8 fs. The RT spectral data were Hann windowed (eq 12) before Fourier transform and subsequently shifted by the correction to the ZORA eigenvalues, the effect of which is already implicitly included in the LR spectrum, as described in section 2.2.

Figure 5 shows the data for  $[\text{Ru}(\text{NH}_3)_6]^{3+}$ , where ruthenium is in the +3 oxidation state. Here, the spectrum (shifted by  $\Delta =$

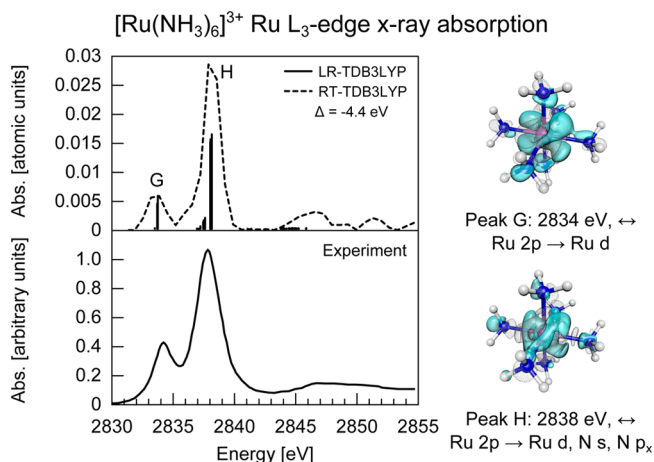


**Figure 5.** Left: (LR/RT)-TDDFT and experimental  $[\text{Ru}(\text{NH}_3)_6]^{3+}$   $L_3$ -edge spectra. Right: Charge density difference snapshots (blue positive, wireframe negative) at an oscillation maximum for two electronic wavepackets after resonant excitation (isovalue  $6 \times 10^{-9}$  au). Peak G involves an excitation to nonbonding  $t_{2g}$  orbitals with in-phase excited state charge density oscillations, whereas peak H involves excitations to antibonding  $e_g$  orbitals with out-of-phase charge oscillations. Experimental data were digitized from ref 49.

$-4.4$  eV) agrees well with experimental results<sup>49</sup> across the energy range shown and is dominated by two large peaks, each of which arises from multiple similar absorptions of differing polarizations, which split in energy due to slight asymmetries in the molecular structure. This is not reflected in the RT-TDDFT spectrum, since symmetry was assumed and only a single  $x$ -polarized simulation was performed. Even if  $x$ ,  $y$ , and  $z$  contributions to the polarizability were performed, the splitting would be too small to resolve. The absence of high energy peaks in the LR spectrum is due to the finite energy window. Both peak G at 2834 eV and peak H at 2838 eV correspond to Ru p  $\rightarrow$  Ru d excitations with a relatively minor influence from the ammine ligands. For resonant excitation, we found an  $x$ -polarized Hann pulse with  $\Delta t = 0.006$  au = 0.15 as,  $\kappa = 0.01$  au,  $t_0 = 60$  au = 1.5 fs, and  $\sigma = 2t_0$  yielded an adequate, effectively monochromatic, excitation. Charge difference densities illustrate the subtle differences between these two excitations. Peak G arises from 2p  $\rightarrow$  4d  $t_{2g}$  orbitals that are nonbonding in character, whereas peak H arises from excitations to antibonding-like  $e_g$  orbitals. The energy difference between these two virtual states is a function of the ligand-field splitting for this octahedral complex. For peak G, this manifests in the excited state charge density as in-phase charge oscillations around the  $\text{NH}_3$  ligands along the  $x$  as well as one orthogonal direction  $z$ , and out-of-phase oscillations for the  $y$  ligands. Peak H, in contrast, involves out-of-phase oscillations on the  $x$  ligands and in-phase oscillations for both orthogonal ( $y$ ,  $z$ ) ligands.



**3.3. Trends in Fluorobenzenes.** Often it is not individual spectra of molecules that are interesting, but rather trends or shifts (e.g., effects of substitution of atoms, functionalization, etc). Here, we model the classic effect of fluorination on the X-ray absorption of benzene. Previous Hartree–Fock<sup>62</sup> and DFT<sup>63</sup> studies have been applied to the C K-edge of fluorobenzene, but to our knowledge this is the first application of TDDFT to the carbon and fluorine K-edges of the complete fluorobenzene series. Figure 6 shows the linear-response

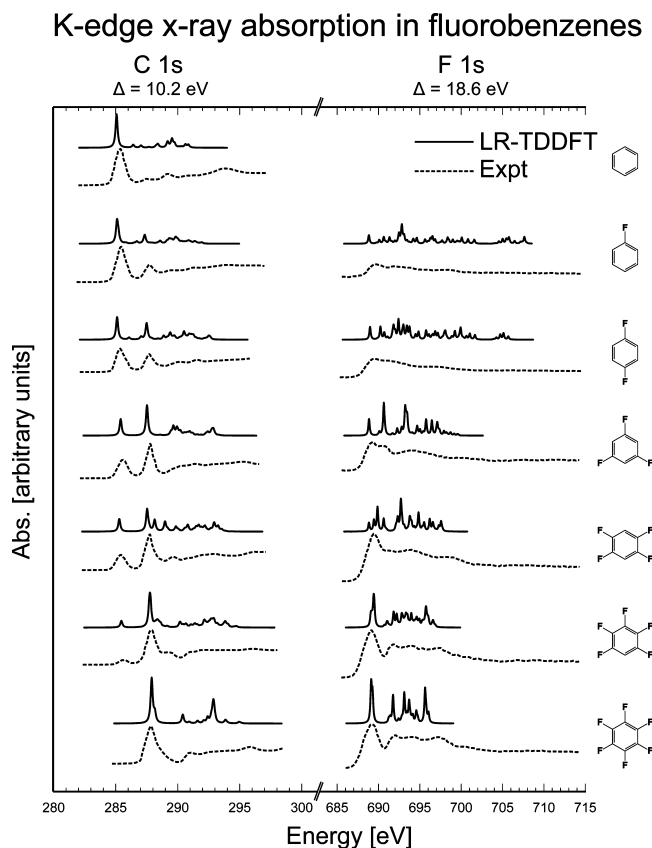


**Figure 6.** Carbon and fluorine K-edge absorption spectra for a range of fluorobenzenes. Upon fluorination, the C 1s  $\rightarrow \pi^*$  transition splits into two peaks, arising from excitations from fluorinated and non-fluorinated carbon atoms. Likewise, the F 1s  $\rightarrow \pi^*$  transition increases in amplitude with increasing fluorination. The experimental data were digitized from ref 48 and normalized to a uniform scale.

spectra along with experimental gas phase data<sup>48</sup> for a series of fluorobenzenes. For each molecule, the geometry was optimized at the aug-cc-pVTZ/B3LYP level, and the TD-B3LYP absorption spectrum was calculated using the Sapporo-TVP+diffuse basis set. Here, we show only linear response calculations, and instead of full TDDFT, we used the Tamm-Dancoff approximation. Our experience has shown that for core states TDDFT and TDA give virtually identical spectra, which is consistent with previous work.<sup>64</sup> The C 1s TDDFT spectra were Lorentzian broadened by 0.2 eV and shifted by  $\Delta = +10.2$  eV to match the lowest excitation in  $C_6F_6$ . The F 1s spectra were similarly broadened and shifted by  $\Delta = +18.6$  eV.

Overall, there is reasonable agreement between the theory and experimental trends, and the peak splittings and amplitudes are consistently captured by TDDFT. Looking first at the carbon K-edge spectra, the isolated strong peak at  $\sim 285$  eV for  $C_6H_6$ , where all carbon atoms are equivalent, is due to a C 1s  $\rightarrow$

$\pi^*$  transition. Upon fluorination, a blue-shifted peak appears, which arises from the same transition, only from carbon atoms bound to an electron-withdrawing fluorine atom, which lowers the carbon 1s eigenvalue by  $\sim 2$  eV. On the basis of Mulliken charge analysis, carbon atoms in  $C_6F_6$ , for example, have  $\sim 0.9$  less electronic charge than in  $C_6H_6$ , and generally speaking, for each species in the series the fluorinated carbon atoms have approximately one less electron than the nonfluorinated atoms. In the  $C_6H_3F_3$  spectrum, there are exactly two types of carbon atoms and thus two clear absorption peaks. These two types of peaks are further split into bands when in nonequivalent carbon atoms, e.g., in  $C_6H_5F$ , there are three types of transition from carbon atoms bonded to hydrogen atoms: from the C atoms ortho, meta, and para to the F-bonded C atom. These splittings are small ( $\sim 0.05$  eV), however, and hidden by the broadening. The relative intensities of the fluorinated and nonfluorinated C atom bands scale with increasing fluorination. Additionally, there is a subtle blue-shift of both bands with increasing fluorination as a consequence of the reduced overall electron density in the carbon backbone, and the correspondingly lowered 1s eigenvalues of both types of carbon atoms. This effect is counteracted somewhat by a reduction in the  $\pi^*$  virtual orbital energy, resulting in an  $\sim 0.5$  eV shift for the nonfluorinated band in going from  $C_6H_6$  to  $C_6HF_5$ . The higher energy bands, which have more complex structure, correspond to excitations from C 1s to higher virtual orbitals.

The fluorine K-edge results tell a similar story. The faint peak at  $\sim 689$  eV in the  $C_6H_5F$  spectrum, which arises from a F 1s  $\rightarrow \pi^*$  transition, increases in intensity with increased fluorination. For each molecule, there is only one type of fluorine atom, and therefore all peaks are distinct (i.e., no bands), except for  $C_6HF_5$ , where there are three different types of F with splittings on the order of 0.1 eV (hidden by broadening). In all but the  $C_6H_2F_4$  molecule, the lower of the two 1s  $\rightarrow \pi^*$  transitions has negligible oscillator strength and is thus absent from the spectra. In  $C_6H_2F_4$ , both peaks are present and the integrated peak area obeys the trend of increased intensity with fluorination. The  $\pi^*$  virtual orbitals, which do not involve the F atoms, are relatively insensitive to fluorination (vary by  $\sim 0.5$  eV at most), and thus the peaks do not appreciably shift down the series.

As compared to the C K-edge spectra, the F spectra are considerably more complex, with densely packed transitions from F 1s to higher virtual orbitals. With increasing fluorination, the density of these spectral features increases, as electron-withdrawing effects result in contraction of the virtual orbital spacings.

#### 4. CONCLUSIONS

In summary, we have outlined our implementation and application of restricted excitation window (REW) linear-response and real-time TDDFT to core-level near-edge X-ray absorption spectroscopy. The computed spectra agree well with experimental results, requiring only a uniform shift ranging from  $-4$  eV to  $+19$  eV, i.e., on the order of a few percent of the excitation energy. Additionally, the excited state charge densities for a few absorption peaks of interest were computed, which visually reveal the nature of the bonding atoms on the absorption, which is particularly illuminating for the subtle effects of the ligands on the  $[Ru(NH_3)_6]^{3+}$  core absorptions. The X-ray absorption spectra for a range of fluorobenzenes are likewise in good agreement with experimental spectra. In short, REW-TDDFT and RT-TDDFT, which require only a small

uniform shift to the absorption spectrum to match experimental results, offer a flexible and predictive approach to core-level excitations, without resorting to tailored initial core-hole states or potentials.

There are a few limitations of the approach worth noting. First, for the high energies involved in the ruthenium complexes, the wavelength of exciting light is on the order of the size of the molecule (e.g.,  $\omega = 2843 \text{ eV} \leftrightarrow \lambda = 4.4 \text{ \AA}$ ), which means that terms beyond the dipole (e.g., quadrupole) become significant in the field–molecule coupling. We found that even if these effects are neglected the results are found to be in good agreement with experimental results, which is reasonable as the excitations are largely confined to the ruthenium and its neighboring atoms, and the applied field is roughly constant over this region. For higher energies, however, such as the K-edge of transition metals, these terms must be included.<sup>43,44</sup> On a related note, for many heavy elements, spin–orbit effects are crucial, and computing the  $L_2$ -edge, for example, requires a full spin–orbit treatment using TDDFT. Though somewhat cumbersome in a linear-response formalism, it is straightforward in a real-time TDDFT approach since it requires only propagating a super density matrix, with the spin–orbit coupling entering as off-diagonal blocks in the one-electron part of the Fock matrix. Real-time studies with spin–orbit ZORA are currently underway. On a final note, the lack of physical peak shapes seriously detracts from the quality of spectra, especially for excitations to higher virtuals (e.g., the fluorobenzene series). The inclusion of nuclear motion via molecular dynamics trajectories can be used to compute lineshapes without phenomenological parameters,<sup>56</sup> and in this spirit real-time coupled electron–nuclear dynamics offers a promising path toward spectra with realistic physical lineshapes.

## AUTHOR INFORMATION

### Corresponding Author

\*E-mail: kenneth.lopatka@pnnl.gov; niri.govind@pnnl.gov.

### Notes

The authors declare no competing financial interest.

## ACKNOWLEDGMENTS

A portion of the research was performed using EMSL, a national scientific user facility sponsored by the U.S. Department of Energy's Office of Biological and Environmental Research and located at Pacific Northwest National Laboratory (PNNL). PNNL is operated for the Department of Energy by the Battelle Memorial Institute under Contract DE-AC06-76RLO-1830. K.L. acknowledges the William Wiley Postdoctoral Fellowship from EMSL. B.E.V.K. and M.K. were supported by the Office of Basic Energy Sciences of the U.S. Department of Energy Grant No. DE-SC0002190 and acknowledge computer time at EMSL (Chinook super-computer) provided via EMSL user proposal 45992. Discussions with Micah Prange and helpful comments from the reviewers are gratefully acknowledged.

## REFERENCES

- (1) Stöhr, J. *NEXAFS Spectroscopy*; Springer: New York, 2003; pp 8–47.
- (2) de Groot, F.; Kotani, A. *Core Level Spectroscopy of Solids*; CRC Press: Boca Raton, FL, 2008; pp 1–37, 457–462.
- (3) Rehr, J. J.; Albers, R. C. *Rev. Mod. Phys.* **2000**, *72*, 621–654.
- (4) Rehr, J.; Ankudinov, A. *Coord. Chem. Rev.* **2005**, *249*, 131–140.

- (5) Pham, V.; Tavernelli, I.; Milne, C.; van der Veen, R.; D'Angelo, P.; Bressler, C.; Chergui, M. *Chem. Phys.* **2010**, *371*, 24–29.
- (6) Atta-Fynn, R.; Johnson, D.; Bylaska, E.; Ilton, E.; Schenter, G.; de Jong, W. *Inorg. Chem.* **2012**, *51*, 3016–3024.
- (7) Ågren, H.; Carravetta, V.; Vahtras, O.; Pettersson, L. *Chem. Phys. Lett.* **1994**, *222*, 75–81.
- (8) Villaume, S.; Ekstrom, U.; Ottosson, H.; Norman, P. *Phys. Chem. Chem. Phys.* **2010**, *12*, 5596–5604.
- (9) Triguero, L.; Pettersson, L. G. M.; Ågren, H. *Phys. Rev. B* **1998**, *58*, 8097–8110.
- (10) Cavalleri, M.; Ogasawara, H.; Pettersson, L.; Nilsson, A. *Chem. Phys. Lett.* **2002**, *364*, 363–370.
- (11) Iannuzzi, M.; Hutter, J. *Phys. Chem. Chem. Phys.* **2007**, *9*, 1599–1610.
- (12) Prendergast, D.; Galli, G. *Phys. Rev. Lett.* **2006**, *96*, 215502.
- (13) Ray, K.; DeBeer George, S.; Solomon, E.; Wieghardt, K.; Neese, F. *Chem.—Eur. J.* **2007**, *13*, 2783–2797.
- (14) Stener, M.; Fronzoni, G.; de Simone, M. *Chem. Phys. Lett.* **2003**, *373*, 115–123.
- (15) Besley, N.; Asmuruf, F. *Phys. Chem. Chem. Phys.* **2010**, *12*, 12024–12039.
- (16) Liang, W.; Fischer, S. A.; Frisch, M. J.; Li, X. *J. Chem. Theory Comput.* **2011**, *7*, 3540–3547.
- (17) Akama, T.; Nakai, H. *J. Chem. Phys.* **2010**, *132*, 054104.
- (18) Casida, M. E. Time-dependent density functional response theory for molecules. In *Recent Advances in Density Functional Methods*; Chong, D. P., Ed.; World Scientific Publishing: River Edge, NJ, 1995; Vol. 1, Chapter 5, pp 155–192.
- (19) Hirata, S.; Head-Gordon, M. *Chem. Phys. Lett.* **1999**, *302*, 375–382.
- (20) Hirata, S.; Head-Gordon, M. *Chem. Phys. Lett.* **1999**, *314*, 291–299.
- (21) Bauernschmitt, R.; Häser, M.; Treutler, O.; Ahlrichs, R. *Chem. Phys. Lett.* **1997**, *264*, 573–578.
- (22) Bauernschmitt, R.; Ahlrichs, R. *Chem. Phys. Lett.* **1996**, *256*, 454–464.
- (23) Stratmann, R.; Scuseria, G.; Frisch, M. J. *Chem. Phys.* **1998**, *109*, 8218.
- (24) *Time-Dependent Density Functional Theory (Lecture Notes in Physics)*, 1st ed.; Marques, M. A.; Ullrich, C. A.; Nogueira, F.; Rubio, A.; Burke, K.; Gross, E. K. U., Eds.; Springer: New York, 2006.
- (25) Valiev, M.; Bylaska, E. J.; Govind, N.; Kowalski, K.; Straatsma, T. P.; Van Dam, H. J. J.; Wang, D.; Nieplocha, J.; Apra, E.; Windus, T. L.; de Jong, W. A. *Comput. Phys. Commun.* **2010**, *181*, 1477–1489.
- (26) NWChem. <http://www.nwchem-sw.org> (accessed June 2012).
- (27) Tretiak, S.; Isborn, C.; Niklasson, A.; Challacombe, M. *J. Chem. Phys.* **2009**, *130*, 054111.
- (28) van Lenthe, E.; Baerends, E. J.; Snijders, J. G. *J. Chem. Phys.* **1994**, *101*, 9783–9792.
- (29) Fronzoni, G.; Stener, M.; Decleva, P.; Wang, F.; Ziegler, T.; van Lenthe, E.; Baerends, E. *Chem. Phys. Lett.* **2005**, *416*, 56–63.
- (30) Nichols, P.; Govind, N.; Bylaska, E.; De Jong, W. J. *J. Chem. Theory Comput.* **2009**, *9*, 491–499.
- (31) Theilhaber, J. *Phys. Rev. B* **1992**, *46*, 12990–13003.
- (32) Yabana, K.; Bertsch, G. F. *Phys. Rev. B* **1996**, *54*, 4484–4487.
- (33) Castro, A.; Appel, H.; Oliveira, M.; Rozzi, C. A.; Andrade, X.; Lorenzen, F.; Marques, M. A. L.; Gross, E. K. U.; Rubio, A. *Phys. Status Solidi B* **2006**, *243*, 2465–2488.
- (34) Jakowski, J.; Morokuma, K. *J. Chem. Phys.* **2009**, *130*, 224106.
- (35) Li, X.; Smith, S.; Markevitch, A.; Romanov, D.; Levis, R.; Schlegel, H. *Phys. Chem. Chem. Phys.* **2005**, *7*, 233–239.
- (36) Takimoto, Y.; Vila, F. D.; Rehr, J. J. *J. Chem. Phys.* **2007**, *127*, 154114.
- (37) Sun, J.; Song, J.; Zhao, Y.; Liang, W.-Z. *J. Chem. Phys.* **2007**, *127*, 234107.
- (38) Meng, S.; Kaxiras, E. *J. Chem. Phys.* **2008**, *129*, 054110.
- (39) Baer, R.; Neuhauser, D. *J. Chem. Phys.* **2004**, *121*, 9803–9807.
- (40) Isborn, C. M.; Li, X. *J. Chem. Phys.* **2008**, *129*, 204107.



- (41) Cheng, C.-L.; Evans, J. S.; Van Voorhis, T. *Phys. Rev. B* **2006**, *74*, 155112.
- (42) Lopata, K.; Govind, N. *J. Chem. Theory Comput.* **2011**, *7*, 1344–1355.
- (43) DeBeer George, S.; Petrenko, T.; Neese, F. *J. Phys. Chem. A* **2008**, *112*, 12936–12943.
- (44) Van Kuiken, B. E.; Khalil, M. *J. Phys. Chem. A* **2011**, *115*, 10749–10761.
- (45) Castro, A.; Marques, M. A. L.; Rubio, A. *J. Chem. Phys.* **2004**, *121*, 3425–3433.
- (46) Wilson, K.; Rude, B.; Catalano, T.; Schaller, R.; Tobin, J.; Dick, T.; Saykally, R. *J. Phys. Chem. B* **2001**, *105*, 3346–3349.
- (47) Domke, M.; Xue, C.; Puschmann, A.; Mandel, T.; Hudson, E.; Shirley, D.; Kaindl, G. *Chem. Phys. Lett.* **1990**, *173*, 122–128.
- (48) Hitchcock, A.; Fischer, P.; Gedanken, A.; Robin, M. *J. Phys. Chem.* **1987**, *91*, 531–540.
- (49) Alperovich, I.; Smolentsev, G.; Moonshiram, D.; Jurss, J. W.; Concepcion, J. J.; Meyer, T. J.; Soldatov, A.; Pushkar, Y. *J. Am. Chem. Soc.* **2011**, *133*, 15786–15794.
- (50) Becke, A. D. *J. Chem. Phys.* **1993**, *98*, 1372–1377.
- (51) Stephens, P. J.; Devlin, F. J.; Chabalowski, C. F.; Frisch, M. J. *J. Phys. Chem.* **1994**, *98*, 11623–11627.
- (52) Lopata, K.; Reslan, R.; Kowalska, M.; Neuhauser, D.; Govind, N.; Kowalski, K. *J. Chem. Theory Comput.* **2011**.
- (53) Yanai, T.; Tew, D. P.; Handy, N. C. *Chem. Phys. Lett.* **2004**, *393*, 51–57.
- (54) Noro, T.; Sekiya, M.; Koga, T. *Theor. Chem. Acc.* **2012**, *131*, 1–8.
- (55) Sapporo Segmented Gaussian Basis Sets. <http://setani.sci.hokudai.ac.jp/sapporo> (accessed June 2012).
- (56) Uejio, J. S.; Schwartz, C. P.; Saykally, R. J.; Prendergast, D. *Chem. Phys. Lett.* **2008**, *467*, 195–199.
- (57) Sham, T. K. *J. Am. Chem. Soc.* **1983**, *105*, 2269–2273.
- (58) de Groot, F.; Hu, Z.; Lopez, M.; Kaindl, G.; Guillot, F.; Tronc, M. *J. Chem. Phys.* **1994**, *101*, 6570.
- (59) Campbell, L.; Mukamel, S. *J. Chem. Phys.* **2004**, *121*, 12323–12333.
- (60) Van Kuiken, B. E.; Huse, N.; Cho, H.; Strader, M. L.; Lynch, M. S.; Schoenlein, R. W.; Khalil, M. *J. Phys. Chem. Lett.* **2012**, *3*, 1695–1700.
- (61) Neese, F. *WIREs Comput. Mol. Sci.* **2012**, *2*, 73–78.
- (62) Cooney, R. R.; Urquhart, S. G. *J. Phys. Chem. B* **2004**, *108*, 18185–18191.
- (63) Triguero, L.; Plashkevych, O.; Pettersson, L.; Ågren, H. *J. Electron. Spectrosc.* **1999**, *104*, 195–207.
- (64) DeBeer George, S.; Neese, F. *Inorg. Chem.* **2010**, *49*, 1849–1853.